Submitted to
ASME Journal of Computational and Nonlinear Dynamics

# LAMINATED COMPOSITE SHELL ELEMENT USING ABSOLUTE NODAL COORDINATE FORMULATION AND ITS APPLICATION TO ANCF TIRE MODEL

*Hiroki Yamashita*
*Department of Mechanical and Industrial Engineering*
*The University of Iowa*
*2312 Seamans Center*
*Iowa City, IA 52242*

*Paramsothy Jayakumar*
*US Army TARDEC*
*6501 E. 11 Mile Road*
*Warren, MI 48397-5000*

*Hiroyuki Sugiyama*
*Department of Mechanical and Industrial Engineering*
*The University of Iowa*
*2416C Seamans Center*
*Iowa City, IA 52242*
*hiroyuki-sugiyama@uiowa.edu*

# Report Documentation Page

*Form Approved*
*OMB No. 0704-0188*



| 1. REPORT DATE | 2. REPORT TYPE | 3. DATES COVERED |
|---|---|---|
| **24 APR 2015** | | **00-00-2015 to 00-00-2015** |

| 4. TITLE AND SUBTITLE | 5a. CONTRACT NUMBER |
|---|---|
| **Laminated Composite Shell Element Using Absolute Nodal Coordinate formulation and its Application to ANCF Tire Model** | 5b. GRANT NUMBER |
| | 5c. PROGRAM ELEMENT NUMBER |
| 6. AUTHOR(S) | 5d. PROJECT NUMBER |
| | 5e. TASK NUMBER |
| | 5f. WORK UNIT NUMBER |
| 7. PERFORMING ORGANIZATION NAME(S) AND ADDRESS(ES) **US Army RDECOM-TARDEC,6501 E. 11 Mile Road,Warren,MI,48397-5000** | 8. PERFORMING ORGANIZATION REPORT NUMBER |
| 9. SPONSORING/MONITORING AGENCY NAME(S) AND ADDRESS(ES) | 10. SPONSOR/MONITOR'S ACRONYM(S) |
| | 11. SPONSOR/MONITOR'S REPORT NUMBER(S) |

12. DISTRIBUTION/AVAILABILITY STATEMENT
**Approved for public release; distribution unlimited**

13. SUPPLEMENTARY NOTES
**Submitted to ASME Journal of Computational and Nonlinear Dynamics**

14. ABSTRACT
**See Report**

15. SUBJECT TERMS

| 16. SECURITY CLASSIFICATION OF: | | | 17. LIMITATION OF ABSTRACT | 18. NUMBER OF PAGES | 19a. NAME OF RESPONSIBLE PERSON |
|---|---|---|---|---|---|
| a. REPORT **unclassified** | b. ABSTRACT **unclassified** | c. THIS PAGE **unclassified** | **Same as Report (SAR)** | **45** | |

## ABSTRACT

In this investigation, a laminated composite shell element of the absolute nodal coordinate formulation (ANCF) is developed for application to the modeling of fiber-reinforced rubber (FRR) structure of the physics-based ANCF tire model. The complex deformation coupling exhibited in fiber-reinforced composite materials can be automatically considered in the shear deformable laminated composite shell element using the continuum mechanics approach, and the element lockings are systematically eliminated by the assumed natural strain and enhanced strain approaches, thereby leading to a locking-free shear deformable ANCF composite shell element. Furthermore, various nonlinear material models can be considered for each layer in a way same as solid elements. Using the ANCF composite shell element developed, a physics-based ANCF tire model is developed by considering the detailed tire geometry and material properties. The experimental validation of the tire model is conducted for the load-deflection curve to ensure that the fundamental structural tire properties can be correctly captured in the ANCF tire model.

## 1. INTRODUCTION

An accurate modeling of the complex tire geometry and the anisotropic material properties of tire structure is essential to the tire performance evaluation including the tire contact pressure and the braking/traction and cornering forces. Since a tire consists of layers of plies and steel belts embedded in rubber, the tire structure needs to be modeled by cord-rubber composite materials and various fiber-reinforced rubber material models are proposed for use in detailed finite element tire models. Since Young's modulus of the steel cord is significantly higher than that of the rubber matrix, mechanical property of the fiber-reinforced rubber (FRR) is highly nonlinear [1]. In particular, the tire cross-section property is of significant importance in characterizing the normal contact pressure distribution. Furthermore, the in-plane shear deformation of the carcass contributes to the cornering characteristics of tires. For this reason, high-fidelity finite element tire models that account for the tire geometric and material nonlinearities are developed and used for the tire performance evaluation [2,3]. However, existing finite element tire models cannot be integrated into the vehicle dynamics simulation due to the essential difference in formulations and solution procedures used in multibody dynamics and nonlinear finite element codes. This prevents an integration of the high-fidelity tire model into the multibody vehicle dynamics simulation [4] and, therefore, the structural characteristics of tires and the transient tire dynamics are, in general, evaluated using different computational models and different simulation approaches. To overcome this fundamental and essential problem in the tire dynamics simulation, a tire model based on the flexible multibody dynamics approach [4-6] is developed using the absolute nodal coordinate formulation (ANCF [7, 8]). The in-plane ANCF-LuGre tire model developed for the transient braking analysis allows for considering the nonlinear coupling between the dynamic structural deformation of the tire and its transient tire force in the contact

patch using general multibody dynamics computer algorithms [6]. The generalization of the in-plane ANCF tire model to the three-dimensional model requires the development of the new ANCF shell element suited for the tire model, which allows for modeling the nonlinear fiber-reinforced rubber materials and the accurate three-dimensional stresses under various maneuvering scenarios. To this end, the continuum mechanics based shear deformable shell element of the absolute nodal coordinate formulation (ANCF) [9] is generalized to a laminated composite shell element in this study for application to the modeling of fiber-reinforced rubber (FRR) structure of the physics-based ANCF tire model. Furthermore, a physics-based ANCF structural tire model is developed using the shear deformable laminated composite shell elements. The paper that discusses the development of the ANCF laminated composite shell element and the physics-based ANCF structural tire model is organized as follows. In Section 2, the kinematics and elastic force formulation of the shear deformable ANCF shell element are overviewed and the procedure for eliminating the element lockings is explained. The classical lamination theory and the generalization of the ANCF shell element to the laminated composite shell element are discussed in Section 3. In Section 4, numerical results and comparison with analytical solutions and existing composite shell elements are presented to validate the ANCF laminated composite shell element developed in this study. Modeling of the physics-based ANCF tire model using the ANCF laminated composite shell element is discussed in Section 5, and comparison with measurement results are presented for validation. Summary and conclusions drawn from this study are presented in Section 6.

## 2. CONTINUUM MECHANICS BASED SHEAR DEFORMABLE ANCF SHELL ELEMENT

### 2.1 Kinematics of ANCF Shell Element

As shown in Fig. 1, the global position vector $\mathbf{r}^i$ of a material point $\mathbf{x}^i = [x^i \quad y^i \quad z^i]^{\mathrm{T}}$ in shell element *i* is defined as [9]

$$\mathbf{r}^i = \mathbf{r}_m^i(x^i, y^i) + z^i \frac{\partial \mathbf{r}^i}{\partial z^i}(x^i, y^i) \tag{1}$$

where $\mathbf{r}_m^i(x^i, y^i)$ is the global position vector in the middle surface and $\partial \mathbf{r}^i(x^i, y^i)/\partial z^i$ is the transverse gradient vector used to describe the orientation and deformation of the infinitesimal volume in the element. Using the bi-linear polynomials, the position vector in the middle surface and the transverse gradient vector are approximated as follows:

$$\mathbf{r}_m^i(x^i, y^i) = \mathbf{S}_m^i(x^i, y^i)\mathbf{e}_p^i, \qquad \frac{\partial \mathbf{r}^i}{\partial z^i}(x^i, y^i) = \mathbf{S}_m^i(x^i, y^i)\mathbf{e}_g^i \tag{2}$$

where $\mathbf{S}_m^i = \begin{bmatrix} S_1^i\mathbf{I} & S_2^i\mathbf{I} & S_3^i\mathbf{I} & S_4^i\mathbf{I} \end{bmatrix}$ and

$$S_1^i = \frac{1}{4}\left(1-\xi^i\right)\left(1-\eta^i\right),\ S_2^i = \frac{1}{4}\left(1+\xi^i\right)\left(1-\eta^i\right),\ S_3^i = \frac{1}{4}\left(1+\xi^i\right)\left(1+\eta^i\right),\ S_4^i = \frac{1}{4}\left(1-\xi^i\right)\left(1+\eta^i\right) \tag{3}$$

where $\xi^i = 2x^i / \ell^i$ and $\eta^i = 2y^i / w^i$. $\ell^i$ and $w^i$ are lengths along the element $x^i$ and $y^i$ axes, respectively. In Eq. 2, the vectors $\mathbf{e}_p^i$ and $\mathbf{e}_g^i$ represent the element nodal coordinates associated with the global position vector in the middle surface and the transverse gradient vector. That is, for node *k* of element *i*, one has $\mathbf{e}_p^{ik} = \mathbf{r}^{ik}$ and $\mathbf{e}_g^{ik} = \partial \mathbf{r}^{ik} / \partial z^i$.

In the continuum mechanics approach, the elastic forces of the shell element are evaluated as a continuum volume and the Green-Lagrange strain tensor **E** at an arbitrary material point in

element *i* is defined as follows:

$$\mathbf{E}^i = \frac{1}{2}\left((\mathbf{F}^i)^T\mathbf{F}^i - \mathbf{I}\right) \tag{4}$$

where $\mathbf{F}^i$ is the global position vector gradient tensor. The preceding equation can be expressed in terms of the covariant strain tensor $\tilde{\mathbf{E}}^i$ as

$$\mathbf{E}^i = (\mathbf{J}^i)^{-T}\tilde{\mathbf{E}}^i(\mathbf{J}^i)^{-1} \tag{5}$$

where $\mathbf{J}^i = \partial\mathbf{X}^i/\partial\mathbf{x}^i$ and $\mathbf{X}^i$ represents the global position vector of element *i* at an arbitrary reference configuration. The covariant strain tensor is defined as

$$\tilde{\mathbf{E}}^i = \frac{1}{2}\left((\bar{\mathbf{J}}^i)^T\bar{\mathbf{J}}^i - (\mathbf{J}^i)^T\mathbf{J}^i\right) \tag{6}$$

where $\bar{\mathbf{J}}^i = \partial\mathbf{r}^i/\partial\mathbf{x}^i$ . Using Eq. 5, the strain vector $\boldsymbol{\varepsilon}^i = [\varepsilon^i_{xx} \quad \varepsilon^i_{yy} \quad \gamma^i_{xy} \quad \varepsilon^i_{zz} \quad \gamma^i_{xz} \quad \gamma^i_{yz}]^T$ is defined as

$$\boldsymbol{\varepsilon}^i = (\mathbf{T}^i)^{-T}\tilde{\boldsymbol{\varepsilon}}^i \tag{7}$$

where $\tilde{\boldsymbol{\varepsilon}}^i$ is the covariant strain vector obtained by Eq. 6, and the constant transformation matrix $\mathbf{T}^i$ is as given in literature [9].

### 2.2 Generalized Elastic Forces

In the continuum mechanics based shear deformable ANCF shell element, element lockings occur due to the use of low-order polynomials, thereby resulting in overly stiff bending behavior. The locking in the bi-linear shear deformable ANCF shell element includes the transverse shear locking; Poisson's thickness locking; curvature thickness locking; in-plane shear locking [9, 10]. These lockings are systematically alleviated by applying the assumed natural strain method [11, 12] and the enhanced assumed strain method [13, 14]. The enhanced strain field for the continuum mechanics-based shear deformable ANCF shell element can then be defined as

follows [9]:

$$\hat{\boldsymbol{\varepsilon}} = \mathbf{T}^{-T}\,\tilde{\boldsymbol{\varepsilon}} + \boldsymbol{\varepsilon}^{EAS} \tag{8}$$

where the covariant transverse normal and shear strains are evaluated by the assumed strain approach, while the other covariant strains are evaluated as compatible strains obtained directly from the assumed global displacement field. This leads to the following covariant strain vector:

$$\tilde{\boldsymbol{\varepsilon}} = \begin{bmatrix} \tilde{\varepsilon}_{xx} & \tilde{\varepsilon}_{yy} & \tilde{\gamma}_{xy} & \tilde{\varepsilon}_{zz}^{ANS} & \tilde{\gamma}_{xz}^{ANS} & \tilde{\gamma}_{yz}^{ANS} \end{bmatrix}^T \tag{9}$$

The enhanced assumed strain vector $\boldsymbol{\varepsilon}^{EAS} = \begin{bmatrix} \varepsilon_{xx}^{EAS} & \varepsilon_{yy}^{EAS} & \gamma_{xy}^{EAS} & \varepsilon_{zz}^{EAS} & 0 & 0 \end{bmatrix}^T$ in Eq. 8 is defined as [13, 14]

$$\boldsymbol{\varepsilon}^{EAS} = \frac{|\mathbf{J}_0|}{|\mathbf{J}(\boldsymbol{\xi})|}\mathbf{T}_0^{-\mathrm{T}}\mathbf{N}(\boldsymbol{\xi})\,\boldsymbol{\alpha} \tag{10}$$

where $\mathbf{J}(\boldsymbol{\xi})$ and $\mathbf{J}_0$ are the global position vector gradient matrices at the reference configuration evaluated at the Gaussian integration point $\boldsymbol{\xi}$ and at the center of element ($\boldsymbol{\xi} = \mathbf{0}$), respectively. $\boldsymbol{\xi}$ is a vector of the element coordinates in the parametric domain and $\mathbf{T}_0$ is the constant transformation matrix evaluated at the center of element. The matrix $\mathbf{N}(\boldsymbol{\xi})$ defines polynomials for the enhancement of the strain field in the parametric domain and $\boldsymbol{\alpha}$ is a vector of internal parameters associated with the interpolating polynomials of the enhanced strain field. The generalized elastic forces of the shell element are obtained as a continuum solid using the virtual work as follows:

$$\mathbf{Q}_s^i = -\int_{V_0^i} \left( \frac{\partial \boldsymbol{\varepsilon}^i}{\partial \mathbf{e}^i} \right)^T \frac{\partial W^i(\hat{\boldsymbol{\varepsilon}}^i)}{\partial \boldsymbol{\varepsilon}^i}\, dV_0^i \tag{11}$$

where $dV_0^i$ is the infinitesimal volume at the reference configuration of element *i*, and $W$ is an elastic energy density function. The continuum mechanics based shear deformable ANCF shell

element allows for considering general hyperelasticity material models in a way same as existing solid elements.

## 3. LAMINATED COMPOSITE SHELL FORMULATION

In fiber-reinforced composite materials that are widely used in many engineering applications, laminae having different fiber angles are bonded together to produce desired material properties. Since many laminae are stacked at different fiber angles, the complex deformation coupling between the extension, shearing, bending and twisting occurs, and such a deformation coupling characterizes the mechanical behavior of fiber-reinforced composite materials [15]. In the first part of this section, the macro-mechanical behavior of fiber-reinforced composite materials is overviewed using the classical lamination theory.

### 3.1 Classical Lamination Theory

In the Kirchhoff plate theory, the plane stress is assumed and the in-plane strains of a plate $\boldsymbol{\varepsilon}_p = [\varepsilon_{xx} \quad \varepsilon_{yy} \quad \gamma_{xy}]^T$ are defined as

$$\boldsymbol{\varepsilon}_p = \boldsymbol{\varepsilon}_p^0 + z\boldsymbol{\kappa} \tag{12}$$

where $\boldsymbol{\varepsilon}_p^0 = [\varepsilon_{xx}^0 \quad \varepsilon_{yy}^0 \quad \gamma_{xy}^0]^T$ is a vector of the in-plane strains in the middle plane, and $\boldsymbol{\kappa} = [\kappa_x \quad \kappa_y \quad \kappa_{xy}]^T$ is a curvature vector associated with bending and twisting. Using a linear orthotropic constitutive law for a fiber-reinforced plate, the in-plane stress vector is related to its strain vector by $\boldsymbol{\sigma}_p = \mathbf{C}_p \boldsymbol{\varepsilon}_p$, and the material moduli is given as [15]

$$\mathbf{C}_p = \mathbf{R}^{-1} \bar{\mathbf{C}}_p \mathbf{R}^{-T} \tag{13}$$

In the preceding equation, the transformation matrix $\mathbf{R}$ is a function of the fiber angle $\theta$ that defines the orientation of the fiber coordinate system *o*-12 with respect to the material frame *o*-*xy*

of the plate as shown in Fig. 1. This matrix is defined by

$$\mathbf{R} = \begin{bmatrix} \cos^2\theta & \sin^2\theta & \sin 2\theta \\ \sin^2\theta & \cos^2\theta & -\sin 2\theta \\ -\sin 2\theta & \sin 2\theta & \cos 2\theta \end{bmatrix} \tag{14}$$

and $\bar{\mathbf{C}}_p$ is the material moduli of an orthotropic material in the fiber coordinate system as

$$\bar{\mathbf{C}}_p = \begin{bmatrix} \bar{C}^{1111} & \bar{C}^{1122} & 0 \\ \bar{C}^{1122} & \bar{C}^{2222} & 0 \\ 0 & 0 & \bar{C}^{1212} \end{bmatrix} \tag{15}$$

where $\bar{C}^{1111} = E_1(1-\nu_{12}\nu_{21})$ , $\bar{C}^{2222} = E_2(1-\nu_{12}\nu_{21})$ , $\bar{C}^{1122} = \nu_{21}E_1(1-\nu_{12}\nu_{21})$ , and $\bar{C}^{1212} = G_{12}$ . While the coupling terms between the normal and shear strains in the fiber coordinate system are zero as observed in Eq. 15, the extension and shear coupling occurs for the stress and strain field defined in the material frame and the coupling terms in the material moduli matrix $\mathbf{C}_p$ of Eq. 13 are not zero. That is, a plate subjected to a uniaxial load produces in-plane shear deformation due to the extension and shear coupling [15]. Using the linear constitutive law for an orthotropic material, the in-plane stresses of a lamina are defined as

$$\boldsymbol{\sigma}_p = \mathbf{C}_p\boldsymbol{\varepsilon}_p^0 + z\,\mathbf{C}_p\boldsymbol{\kappa} \tag{16}$$

The force and moment resultants of a fiber-reinforced composite consisting of *N* orthotropic laminae can then be defined as

$$\mathbf{N} = \sum_{k=1}^{N}\mathbf{C}_p^k\int_{z_{k-1}}^{z_k}\boldsymbol{\varepsilon}_p^0\,dz + \sum_{k=1}^{N}\mathbf{C}_p^k\int_{z_{k-1}}^{z_k} z\,\boldsymbol{\kappa}\,dz \tag{17}$$

and

$$\mathbf{M} = \sum_{k=1}^{N}\mathbf{C}_p^k\left(\int_{z_{k-1}}^{z_k} z\,\boldsymbol{\varepsilon}_p^0\,dz\right) + \sum_{k=1}^{N}\mathbf{C}_p^k\left(\int_{z_{k-1}}^{z_k} z^2\,\boldsymbol{\kappa}\,dz\right) \tag{18}$$

where $\mathbf{N} = [N_x \quad N_y \quad N_{xy}]^T$ , $\mathbf{M} = [M_x \quad M_y \quad M_{xy}]^T$ , $\mathbf{C}_p^k$ is the material moduli matrix of the *k*-

th layer, and $z_k$ is the thickness coordinate at the upper surface of the *k*-th layer. It is important to notice here that the force and moment resultants are defined as forces and moments per unit length [15]. Since the strain and curvature are not function of the thickness coordinate *z* in the Kirchhoff plate theory, Eqs. 17 and 18 are written in a matrix form as [15]

$$\begin{bmatrix} \mathbf{N} \\ \mathbf{M} \end{bmatrix} = \begin{bmatrix} \mathbf{A} & \mathbf{B} \\ \mathbf{B} & \mathbf{D} \end{bmatrix} \begin{bmatrix} \boldsymbol{\varepsilon}_p^0 \\ \boldsymbol{\kappa} \end{bmatrix} \tag{19}$$

where $A_{ij} = \sum_{k=1}^{N} (C_p^k)_{ij} (z_k - z_{k-1})$ , $B_{ij} = \sum_{k=1}^{N} (C_p^k)_{ij} (z_k^2 - z_{k-1}^2)/2$ , and $D_{ij} = \sum_{k=1}^{N} (C_p^k)_{ij} (z_k^3 - z_{k-1}^3)/3$ .

The presence of the matrix **B** implies the extension and bending/twisting coupling of a laminate. However, if each lamina above the mid-plane is identical to that below the mid-plane in both geometry and material properties (i.e., the laminate is mid-plane symmetric), the matrix **B** becomes identically zero (i.e., $B_{ij} = 0$) and the extension and bending/twisting coupling vanishes. It is important to notice here that the extension and shear coupling still exists. Another important case is a balanced laminate, in which a laminate consists of a pair of laminae that have opposite fiber angles ($+\theta$ and $-\theta$) above and below the mid-plane, regardless of the stacking sequence. This eliminates the extension and shear coupling. That is, coupling terms of in-plane normal and in-plane shear strains in matrix **A** are identically zero. For a two-layer laminate with the same layer thickness and opposite fiber angle ($+/-\theta$) about the mid-plane, the extension and shear coupling vanishes, but the extension and twisting coupling in **B** matrix exists. This causes twisting deformation of a laminated composite plate subjected to a uniaxial tensile loading [15]. The presence of such a complex coupling is discussed using the ANCF laminated composite shell element in Section 4.

### 3.2 Generalization to Shear Deformable ANCF Composite Shell Element

As discussed in Section 2, the continuum mechanics based ANCF shell element is formulated as a continuum solid that accounts for the three-dimensional stress state, thus the complex deformation coupling exhibited in laminates can be automatically considered without special elastic force formulations. That is, the generalized elastic force of the laminated composite shell element that consists of *N* layers can be defined as follows:

$$\mathbf{Q}_s^i = -\sum_{k=1}^{N} \int_{V_0^{ik}} \left( \frac{\partial \boldsymbol{\varepsilon}^{ik}}{\partial \mathbf{e}^i} \right)^T \frac{\partial W^{ik}(\hat{\boldsymbol{\varepsilon}}^{ik})}{\partial \boldsymbol{\varepsilon}^{ik}} dV_0^{ik} \tag{20}$$

In the preceding equation, the integration interval for the *k*-th layer in the thickness direction is from $z_{k-1}$ to $z_k$. In other words, the element generalized elastic forces are evaluated layer by layer and the resulting generalized elastic forces of each layer are simply added together to define the elastic force vector of the laminated composite shell. It is important to notice here that there is no restriction in material models considered in each lamina, despite the fact the orthotropic material law is the most popular material model used for reinforced composite materials. Two Gaussian integration points are used along the thickness when the elastic forces of *each* layer are evaluated.

**Orthotropic Saint-Venant-Kirchhoff Material Model** For an orthotropic Saint-Venant-Kirchhoff material, the material moduli $C^{ijkl} = \partial^2 W / \partial \varepsilon_{ij} \partial \varepsilon_{kl}$ of a fiber-reinforced lamina in the material frame is defined as [16]

$$C^{ijkl} = (\mathbf{b}^i \cdot \mathbf{a}_a)(\mathbf{b}^j \cdot \mathbf{a}_b)(\mathbf{b}^k \cdot \mathbf{a}_c)(\mathbf{b}^l \cdot \mathbf{a}_d)\bar{C}^{abcd} \tag{21}$$

where $(\mathbf{J}^i)^{-1} = [\mathbf{b}^1 \quad \mathbf{b}^2 \quad \mathbf{b}^3]$ and $\bar{C}^{abcd}$ is the tangent material moduli defined using 9 material parameters in the fiber coordinate system $[\mathbf{a}_1 \quad \mathbf{a}_2 \quad \mathbf{a}_3]$ as shown in Fig. 1, where the direction of

fiber is defined along the coordinate 1. The material moduli $\bar{C}^{abcd}$ in the fiber coordinate system are given as follows [16]:

$$[\bar{C}^{ijkl}] = \begin{bmatrix} \bar{C}^{1111} & \bar{C}^{1122} & 0 & \bar{C}^{1133} & 0 & 0 \\ \bar{C}^{1122} & \bar{C}^{2222} & 0 & \bar{C}^{2233} & 0 & 0 \\ 0 & 0 & \bar{C}^{1212} & 0 & 0 & 0 \\ \bar{C}^{1133} & \bar{C}^{2233} & 0 & \bar{C}^{3333} & 0 & 0 \\ 0 & 0 & 0 & 0 & \bar{C}^{2323} & 0 \\ 0 & 0 & 0 & 0 & 0 & \bar{C}^{1313} \end{bmatrix} \tag{22}$$

where

$$\begin{aligned} &\bar{C}^{1111} = E_1(1-\nu_{23}\nu_{32})/\Delta \quad && \bar{C}^{2222} = E_2(1-\nu_{13}\nu_{31})/\Delta \quad && \bar{C}^{3333} = E_3(1-\nu_{12}\nu_{21})/\Delta \\ &\bar{C}^{1122} = E_1(\nu_{21}+\nu_{31}\nu_{23})/\Delta \quad && \bar{C}^{1133} = E_3(\nu_{13}+\nu_{12}\nu_{23})/\Delta \quad && \bar{C}^{2233} = E_2(\nu_{32}+\nu_{12}\nu_{31})/\Delta \\ &\bar{C}^{1212} = G_{12} && \bar{C}^{2323} = G_{23} && \bar{C}^{1313} = G_{13} \end{aligned} \tag{23}$$

and $\Delta = 1-\nu_{12}\nu_{21}-\nu_{23}\nu_{32}-\nu_{31}\nu_{13}-2\nu_{21}\nu_{32}\nu_{13}$.

**Mooney-Rivlin Material Model** For modeling incompressible materials such as rubbers, Mooney-Rivlin material model is widely used. The energy density function is defined as [17]

$$W = C_1(\bar{I}_1 - 3) + C_2(\bar{I}_2 - 3) + \frac{K}{2}(J-1)^2 \tag{24}$$

where $C_1$ and $C_2$ are material constants, $\bar{I}_1 = I_1/(I_3)^{1/3}$, $\bar{I}_2 = I_2/(I_3)^{2/3}$ and $J = (I_3)^{1/2}$, where $I_1$, $I_2$ and $I_3$ are invariants of right Cauchy-Green tensor [17]. $K$ is a bulk modulus. The second Piola–Kirchhoff stress tensor **S** is obtained by differentiating the energy density function $W$ with respect to Green-Lagrange strain tensor **E** as

$$\mathbf{S} = \frac{\partial W}{\partial \mathbf{E}} = 2C_1\left(I_3\right)^{-1/3}\left(\mathbf{I} - \frac{1}{3}I_1\mathbf{C}^{-1}\right) + 2C_2\left(I_3\right)^{-2/3}\left(I_1\mathbf{I} - \mathbf{C} - \frac{2}{3}I_2\mathbf{C}^{-1}\right) + KJ(\mathrm{J}-1)\mathbf{C}^{-1} \tag{25}$$

**Equations of Motion** Using the principle of virtual work in dynamics, the equations of motion of the shear deformable laminated composite shell element $i$ can be expressed as

$$\mathbf{M}^i\ddot{\mathbf{e}}^i = \mathbf{Q}_s^i(\mathbf{e}^i, \boldsymbol{\alpha}^i) + \mathbf{Q}_e^i(\mathbf{e}^i, \dot{\mathbf{e}}^i, t) \tag{26}$$

where vectors $\mathbf{Q}_s^i$ and $\mathbf{Q}_e^i$ are, respectively, the element elastic and external force vectors; and the matrix $\mathbf{M}^i$ is the constant element mass matrix defined by

$$\mathbf{M}^i = \sum_{k=1}^{N} \int_{V_0^{ik}} \rho_0^{ik} (\mathbf{S}^i)^T \mathbf{S}^i dV_0^{ik} \tag{27}$$

where $\rho_0^{ik}$ is the material density of *k*-th layer at the reference configuration. The internal parameters $\boldsymbol{\alpha}^i$ introduced for the enhanced assumed strains are determined by solving the following equations [13, 14]:

$$\int_{V_0^i} \left( \frac{\partial \boldsymbol{\varepsilon}^{EAS}}{\partial \boldsymbol{\alpha}^i} \right)^T \frac{\partial W^i(\hat{\boldsymbol{\varepsilon}}^i)}{\partial \boldsymbol{\varepsilon}^i} dV_0^i = \mathbf{0} \tag{28}$$

It is important to notice here that the preceding equations can be solved at element level for the unknown internal parameters $\boldsymbol{\alpha}^i$ using the procedure presented in the literature [9].

## 4. NUMERICAL EXAMPLES

### 4.1 Extension and In-Plane Shear Coupling of Fiber-Reinforced Plate Subjected to Uniaxial Tensile Load

To discuss the extension and in-plane shear coupling of a fiber-reinforced material, a uniaxial tension test as shown in Fig 2(a) is considered using the shear deformable ANCF shell element. The length, width and thickness of the plate are 2.0 m, 1.0 m, and 0.01 m, respectively. Young's modulus of the fiber and those of the matrix are, respectively, assumed to be $E_x = 1.8\times10^{11}$ Pa and $E_y = E_z = 1.3333\times10^{7}$ Pa. The shear modulus of rigidity and Poisson's ratio are assumed to be $G_{xy} = \mathrm{G}_{xz} = \mathrm{G}_{yz} = 3.33333\times10^{6}$ Pa and $\nu_{xy} = \nu_{xz} = \nu_{yz} = 0.4$, respectively. The tensile distributed uniaxial load of 5000 N/m is applied in the *X* direction. The in-plane shear strain of

the plate is presented in Fig. 3 as a function of the fiber angle $\theta$. In this figure, the in-plane shear strain obtained by the ANCF composite shell element is compared with the analytical solution given by [1]

$$\gamma_{xy} = \sin 2\theta \left( \frac{\cos^2 \theta}{E_1} - \frac{\sin^2 \theta}{E_2} + \frac{1}{2}\left( \frac{2\nu_{12}}{E_1} - \frac{1}{G_{12}} \right) \cos 2\theta \right) \sigma_x \tag{29}$$

It is observed from the preceding equation that the change in the shear strain is nonlinear in the fiber angle $\theta$. The sign of the shear strain changes at $\theta = 54.7$ degrees [1] as shown by the magnified deformed shapes at $\theta = 20$, 54.7 and 70 degrees in Fig. 3. The results obtained by the ANCF shell element agree well with the analytical solution based on the assumption of Kirchhoff plate theory with infinitesimal deformation. Furthermore, using Eq. 29, the inflection points of the in-plane shear strain are obtained at $\theta = 25.5$ and 71.3 degrees, and they are also well predicted using the ANCF composite shell element.

### 4.2 Warpage of Two-Layer Laminated Composite Plate Subjected to Uniaxial Tensile Load

To validate the ANCF laminated composite shell element, a uniaxial tensile test of a two-layer laminate at $+/-\theta$ fiber angles is considered as shown in Fig. 2 (b) [15]. The length, width and thickness of the plate are same as the previous example in Section 4.1. The thicknesses of each layer is 0.005 m. The fiber angles of the upper and lower layers are same in magnitude, but opposite in direction as shown in Fig. 2 (b). The material properties of each layer are also same as the previous example in Section 4.1. The tensile distributed uniaxial load of 500 N/m is applied in the *X* direction. As discussed in Section 3.1, the extension and bending/twisting coupling described by **B** matrix in Eq. 19 are not zero in this laminate, and it causes the warpage

(twisting) under the uniaxial tensile loading [15]. The extension and shear coupling exists in each lamina. However, shear deformation of the upper and lower layers caused by the uniaxial tensile load are same in magnitude, but opposite in direction. Thus, the shear deformations of both layers are canceled out and no in-plane shearing occurs in the laminated composite. That is, the extension and shear coupling term of **A** matrix of the laminate in Eq. 19 becomes identically zero in this problem.

To demonstrate this fundamental coupling behavior of the laminated composite material using the ANCF laminated composite shell element, the twisting angle and the in-plane shear strain of the two-layer laminated composite plate are presented in Fig. 4 as a function of the fiber angle $\theta$. In this figure, results obtained by the ANCF laminated composite shell element are compared with the analytical model based on the classical lamination theory discussed in Section 3.1. In the analytical model, the warpage is defined by [15]

$$w = -\frac{1}{2}\left(\kappa_x x^2 + \kappa_y y^2 + \kappa_{xy} xy\right) \tag{30}$$

where the curvature vector $\boldsymbol{\kappa} = [\kappa_x \quad \kappa_y \quad \kappa_{xy}]^T$ is determined by solving the following equation:

$$\begin{bmatrix} \boldsymbol{\varepsilon}_p^0 \\ \boldsymbol{\kappa} \end{bmatrix} = \begin{bmatrix} \mathbf{A} & \mathbf{B} \\ \mathbf{B} & \mathbf{D} \end{bmatrix}^{-1} \begin{bmatrix} \mathbf{N} \\ \mathbf{M} \end{bmatrix} \tag{31}$$

for $\mathbf{N} = [N_x \quad 0 \quad 0]^T$ and $\mathbf{M} = [0 \quad 0 \quad 0]^T$. It is observed from Fig. 4 that the twisting angles agree well with those based on the classical lamination theory, and the warpage developed by the uniaxial tensile load applied to the two-layer laminated composite plate is well predicted by the ANCF laminated composite shell element developed in this study. The sign of the twisting angle of the composite plate changes at the fiber angle of $\theta = 54.7$ degrees [1], and this important fiber angle is also correctly predicted with the ANCF laminated composite shell element. Furthermore,

zero in-plane shear strain is ensured in the results obtained by the ANCF laminated composite shell element regardless of the fiber angle, and this result agrees with that of the analytical model based on the classical lamination theory.

### 4.3 Cantilevered Two-Layer Composite Shell Subjected to a Point Load

To demonstrate the accuracy of the ANCF composite shell element for large deformation problem of initially curved shell structures, a cantilevered quarter cylinder modeled by $+/-\theta$ two-layer composite shell is considered as shown in Fig. 5. The fiber angle of each layer is assumed to be $20^{\circ}$. The radius of curvature is assumed to be 1.0 m. The width and height are assumed to be 1.0 m and 0.01 m (i.e., 0.005 m thickness for each layer). Young's modulus of the fiber and those of the matrix are, respectively, assumed to be $E_x = 2.0\times10^8$ Pa and $E_y = E_z = 1.0\times10^8$ Pa. The shear modus of rigidity and Poisson's ratio are assumed to be $G_{xy} = \mathrm{G}_{xz} = \mathrm{G}_{yz} = 3.84615\times10^7$ Pa and $\nu_{xy} = \nu_{xz} = \nu_{yz} = 0.3$, respectively. The vertical point load of 10 N is applied to the corner of the shell as shown in Fig. 5. The deformed shape at the static equilibrium state is shown in Fig. 5, in which the large deformation is exhibited. The static deflections of the load application point obtained by the ANCF laminated composite shell element are compared with those of the shear deformable composite shell element of ANSYS (SHELL181) [17] in Table 1 for different number of elements. It is demonstrated in this Table that good agreements in solution are obtained between the shear deformable laminated composite shell elements obtained by the absolute nodal coordinate formulation and the MITC shell formulation [17] implemented in ANSYS. The numerical convergence of the finite element solutions are presented in Fig. 6 for errors defined by the deviation from the reference solution, where the reference solution of -0.80517 m is obtained by $100\times100$ elements using the ANSYS

SHELL181 composite shell element. It is observed from this figure that the ideal linear rate of convergence is ensured in both models for the large deformation problem and it indicates that element lockings are properly eliminated in the ANCF laminated composite shell element developed in this study.

### 4.4 Natural Frequencies of Laminated Composite Plate

The eigenfrequency analysis of the $+/-\theta$ two-layer composite plate is considered in this example. The fiber angle of each layer is assumed to be $20^{\circ}$. A free boundary condition is assumed. The length, width and thickness of the plate are 1.0 m, 1.0 m, and 0.01 m (i.e., 0.005 m thickness for each layer), respectively. Young's modulus of the fiber and those of the matrix are, respectively, assumed to be $E_x = 6.0\times10^7$ Pa and $E_y = E_z = 3.0\times10^7$ Pa. The shear modus of rigidity and Poisson's ratio are assumed to be $G_{xy} = \mathrm{G}_{xz} = \mathrm{G}_{yz} = 1.1538\times10^7$ Pa and $\nu_{xy} = \nu_{xz} = \nu_{yz} = 0.3$, respectively. The material density is assumed to be 500 kg/m$^3$. The first ten eigenfrequencies and their mode shapes are shown in Table 2 and Fig. 7, respectively. The eignfrequencies are compared with the reference solutions obtained by the $100\times100$ elements using the ANSYS SHELL181 composite shell element. The eigenfrequencies are also well predicted with the ANCF laminated composite shell element.

### 4.5 Quarter Cylinder Pendulum with Laminated Composite Material

In the last numerical example, the nonlinear dynamic analysis of the $+/-\theta$ two-layer laminated composite shell structure (a quarter cylinder pendulum) is discussed as shown in Fig. 8. The radius of curvature is assumed to be 1.0 m. The fiber angle of each layer is assumed to be $20^{\circ}$ and the material property of each layer is same as that of the previous example in Section 4.4.

One corner of the composite quarter cylinder is connected to the ground by a spherical joint. The deformed shapes under the effect of gravity are shown in Fig. 8, in which large deformation is observed. The global *X*, *Y* and *Z* positions at the corner point shown by a red circle in Fig. 8 are presented in Figs. 9, 10 and 11, respectively. Despite the highly nonlinear dynamics problem involving the large deformation of composite materials, the numerical solution obtained by $10\times10$ elements are close to those of $30\times30$ elements.

## 5. APPLICATION TO PHYSICS-BASED ANCF TIRE MODEL

In the numerical examples in the preceding section, the fundamental element performance of the shear deformable ANCF laminated composite shell element developed in this study is demonstrated. Use of the element developed allows for predicting the complex deformation coupling between the extension, shearing, bending and twisting that characterizes the mechanical behavior of fiber-reinforced composite materials. This is an important modeling requirement for developing the physics-based tire model, and use of the absolute nodal coordinate formulation in modeling the tire structure allows for the integration of the flexible tire model into the general multibody dynamics computer algorithms for vehicle dynamics simulation. For this reason, in this section, a modeling procedure of the physics-based ANCF tire model using the ANCF laminated composite shell element is discussed, and the fundamental structural characteristics of the ANCF tire model are validated by comparison with the measurement results of a tire.

A tire has a complex structure that consists of layers of plies and steel belts that are embedded in rubber, thus an accurate modeling of the complex tire geometry and the anisotropic material properties is essential to the tire performance evaluation including the tire contact pressure and the braking/traction and cornering forces. While the in-plane tire belt deformation can be modeled by an equivalent material model [5,6], such a simplified material model cannot be used

for predicting the overall tire structural deformation in the three-dimensional analysis. This is attributed to the fact that the tire section property in both geometry and material is of crucial importance in characterizing the contact pressure distribution. This necessitates various fiber-reinforced rubber material models that can be integrated into high-fidelity finite element tire models [2,3]. However, despite the fact that accurate solutions can be obtained using existing finite element tire models, difficulties arise when they are integrated into the vehicle dynamics simulation due to the essential difference in formulations and solution procedures used in multibody dynamics and nonlinear finite element codes. This prevents an integration of the high-fidelity tire model into the multibody vehicle dynamics simulation.

In order to develop a physics-based absolute nodal coordinate formulation tire model, the tire cross section geometry is imported from the tire cut section and data points are interpolated by a cubic smoothing spline to extract the nodal position and slope coordinates. As shown in Fig. 12, the tire cross-section is divided into the tread, sidewall, and bead sections. The number of layers, cord angles of layers, material properties are provided in each section to create the tire model data as shown in Fig. 13. The tread section consists of a carcass ply, two steel belts, a belt cover, and tread blocks. The carcass ply and steel belt are modeled as an orthotropic material with polyester and steel cords embedded in rubber, respectively. A rubber layer is considered between the upper and lower steel belts and between the carcass ply and the lower steel belt. The sidewall section is modeled by two carcass plies and a rubber that lies in between. The bead section is modeled by two carcass plies, a steel belt, and a rubber as shown in Fig. 13. Having determined the cross-section property, the three-dimensional tire geometry is generated by rotating the tire section model, and the nodal position and slope coordinates of the ANCF tire model are created as summarized in Fig. 12.

The tire considered in the numerical example is 215/45R17. The air pressure of 220 kPa is considered by the normal distributed load applied to the inner surface of the tire. The penalty approach is used for modeling the normal contact force at each node in contact. The load-deflection curve is important for characterizing the fundamental structural properties of tires. The lateral and vertical deflections of the ANCF tire model shown in Fig. 14 are compared with the measurement results in Figs. 15 and 16. It is observed from these figures that the local tire deflections are well predicated in both lateral and vertical directions for the various wheel loads. Furthermore, the lengths of the contact patch in the longitudinal and lateral directions also agree well with those of the measurement results as shown in Fig. 17 and 18.

## 6. SUMMARY AND CONCLUSIONS

In this study, a continuum mechanics based shear deformable shell element of the absolute nodal coordinate formulation (ANCF) is generalized to a laminated composite shell element for application to the modeling of fiber-reinforced rubber (FRR) structure of the physics-based ANCF tire model. It is shown that the complex deformation coupling exhibited in fiber-reinforced composite materials can be automatically considered in the shear deformable laminated composite shell element using the continuum mechanics approach. Furthermore, the element lockings are systematically eliminated by the assumed natural strain and enhanced strain approaches, thereby leading to a locking-free shear deformation ANCF laminated composite shell element. The several benchmark problems are used to validate the ANCF laminated composite shell element with particular emphasis on the deformation coupling exhibited in composite materials. The numerical results are in good agreement with those predicated by the analytical model based on the classical lamination theory and the laminated solid shell element in ANSYS. Furthermore, using the ANCF laminated composite shell element developed, a physics-

based ANCF tire model is developed by considering the detailed tire geometry and anisotropic material properties. The fiber-reinforced rubber is considered for modeling the carcass plies and steel belts using the multi-layered laminated composite shell elements. The load-deflection curves as well as the contact patch sizes predicted by the physics-based ANCF tire model are in good agreement with the measurement results.

## ACKNOWLEDGEMENTS

This research is supported by the Automotive Research Center (ARC) in accordance with Cooperative Agreement W56HZV-04-2-0001 U.S. Army Tank Automotive Research, Development and Engineering Center (TARDEC).

## REFERENCES

[1] Clark, S. K. (ed.), 1981, *Mechanics of Pneumatic Tires*, US DOT HS805 952 NHTSA.

[2] Lee, C.R., Kim, J.W., Hallquist, J.O., Zhang, Y. and Farahani, A.D., 1997, "Validation of a FEA Tire Model for Vehicle Dynamic Analysis and Full Vehicle Real Time Proving Ground Simulations", *SAE Technical Paper 971100*.

[3] Gruber, P., Sharp, R. S. and Crocombe, A. D., 2012, "Normal and Shear Forces in the Contact Patch of a Braked Racing Tyre. Part 2: Development of a Physical Tyre Model", *Vehicle System Dynamics*, vol. 50, pp. 339-356.

[4] Sugiyama, H., Yamashita, H. and Jayakumar, P., 2014, "Right on Tracks - An Integrated Tire Model for Ground Vehicle Simulation", *Tire Technology International*, vol. 67, pp. 52-55.

[5] Sugiyama, H. and Suda, Y., 2009, "Nonlinear Elastic Ring Tire Model Using the Absolute Nodal Coordinate Formulation", *IMechE Journal of Multi-Body Dynamics*, vol. 223, pp. 211-219.

[6] Yamashita, H., Matsutani, Y. and Sugiyama, H., "Longitudinal Tire Dynamics Model for Transient Braking Analysis: ANCF-LuGre Tire Model", *ASME Journal of Computational and Nonlinear Dynamics*, in press. (doi:10.1115/1.4028335)

[7] Shabana, A. A., *Dynamics of Multibody Systems*, 2005, Cambridge University Press, New York.

[8] Gerstmayr, J., Sugiyama, H., and Mikkola, A., 2013, "Review on the Absolute Nodal Coordinate Formulation for Large Deformation Analysis of Multibody Systems", *ASME Journal of Computational and Nonlinear Dynamics*, vol. 8, pp. 031016-1-12.

[9] Yamashita, H., Valkeapää, A., Jayakumar, P. and Sugiyama, H., "Continuum Mechanics Based Bi-Linear Shear Deformable Shell Element using Absolute Nodal Coordinate Formulation", *ASME Journal of Computational and Nonlinear Dynamics*, in press. (doi:10.1115/1.4028657)

[10] Valkeapää, A., Yamashita, H., Jayakumar, P. and Sugiyama, H., "On the Use of Elastic Middle Surface Approach in the Large Deformation Analysis of Moderately Thick Shell Structures using Absolute Nodal Coordinate Formulation", *Nonlinear Dynamics*, in press. (doi: 10.1007/s11071-015-1931-6)

[11] Dvorkin, E. N., and Bathe, K. J., 1984, "A Continuum Mechanics Based Four-Node Shell Element for General Non-Linear Analysis", *Engineering Computations*, vol. 1, pp.77-88.

[12] Betsch, P., and Stein, E., 1995, "An Assumed Strain Approach Avoiding Artificial Thickness Straining for A Non-Linear 4-Node Shell Element", *Communications in Numerical Methods in Engineering*, vol. 11, pp. 899-909.

[13] Simo, J. C., and Rifai, M. S., 1990, "A Class of Mixed Assumed Strain Methods and The Method of Incompatible Modes", *International Journal for Numerical Methods in Engineering*, vol. 29, pp.1595-1638.

[14] Andelfinger, U., and Ramm, E., 1993, "EAS-Elements for Two-Dimensional, Three-Dimensional, Plate and Shell Structures and Their Equivalence to HR-Elements", *International Journal for Numerical Methods in Engineering*, vol. 36, pp.1311-1337.

[15] Jones, R. M., 1999, *Mechanics of Composite Materials*, Taylor and Francis.

[16] Vu-Quoc, L., and Tan, X. G., 2003, "Optimal Solid Shells for Non-Linear Analyses of Multilayer Composites: I Statics", *Computer Methods in Applied Mechanics and Engineering*, vol. 192, pp. 975-1016.

[17] Bathe, K.J., *Finite Element Procedures*, 1996, Prentice Hall.

Table 1. Static deflection of cantilevered two-layer composite shell subjected to point load (m)

| Number of elements | ANCF composite shell | ANSYS composite shell (SHELL181) |
|---|---|---|
| 4×4 | -0.77157 | -0.78262 |
| 8×8 | -0.79931 | -0.79786 |
| 16×16 | -0.80310 | -0.80220 |
| 32×32 | -0.80414 | -0.80619 |
| 50×50 | -0.80452 | -0.80473 |
| 64×64 | -0.80469 | -0.80493 |

Table 2. First ten eigenfrequencies of the ANCF laminated composite shell (Hz)

| ANCF composite shell 2×2 | ANCF composite shell 4×4 | ANCF composite shell 8×8 | ANCF composite shell 16×16 | ANCF composite shell 32×32 | ANSYS composite shell (SHELL181) 100×100 |
|---|---|---|---|---|---|
| 1.8168 | 1.7705 | 1.7385 | 1.7291 | 1.7295 | 1.7175 |
| 2.9444 | 2.6214 | 2.4887 | 2.4518 | 2.4296 | 2.4424 |
| 4.3411 | 3.7085 | 3.4579 | 3.3853 | 3.3642 | 3.3700 |
| 4.8487 | 4.6450 | 4.4097 | 4.3355 | 4.3088 | 4.2951 |
| 5.4240 | 5.0939 | 4.8413 | 4.7605 | 4.7412 | 4.7220 |
| 9.1235 | 9.3139 | 7.7790 | 7.2886 | 7.1604 | 7.1146 |
| 116.4075 | 9.7130 | 8.5528 | 8.3152 | 8.2496 | 8.2005 |
| 127.6218 | 10.7920 | 9.2868 | 8.8343 | 8.7120 | 8.6442 |
| 133.0542 | 12.3383 | 9.8813 | 9.2463 | 9.0973 | 9.0559 |
| 141.4632 | 14.1086 | 11.5408 | 10.8417 | 10.6750 | 10.6080 |

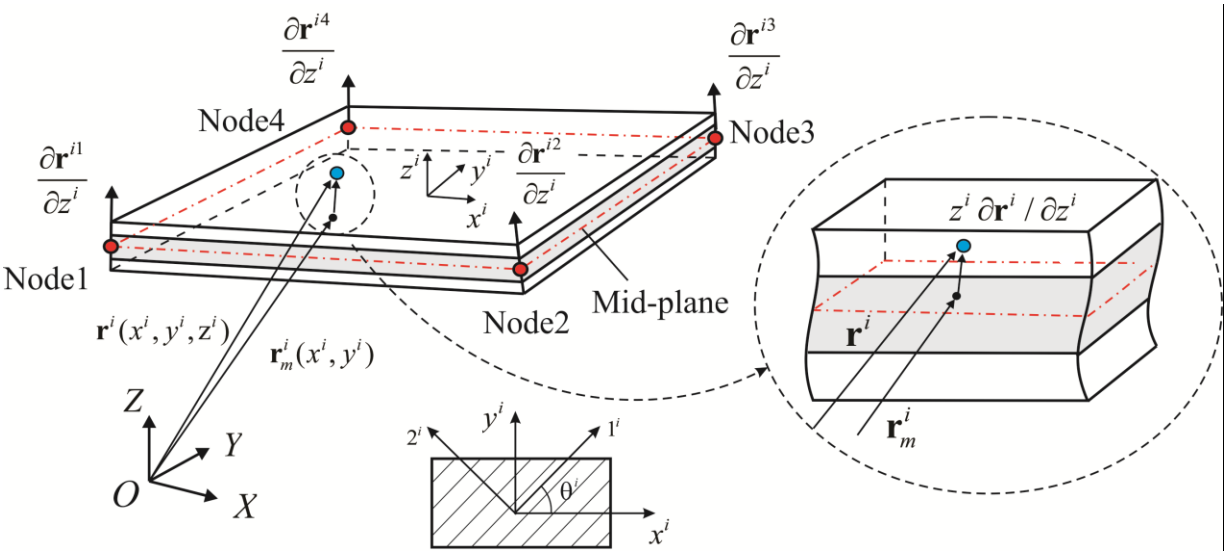


Figure 1. Kinematics of shear deformable ANCF laminated composite shell element

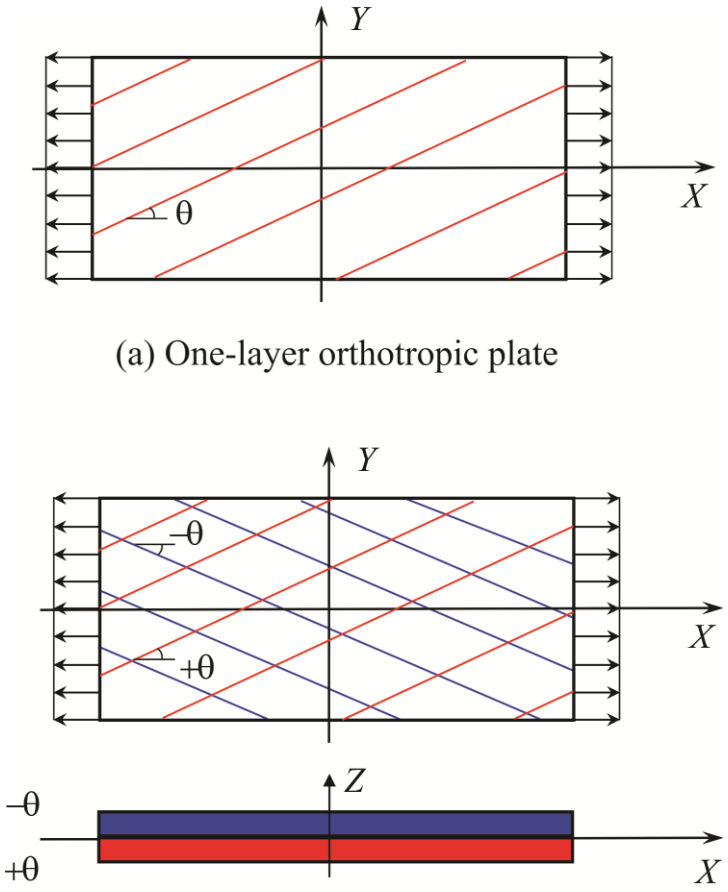


Figure 2. Uniaxial tensile test models

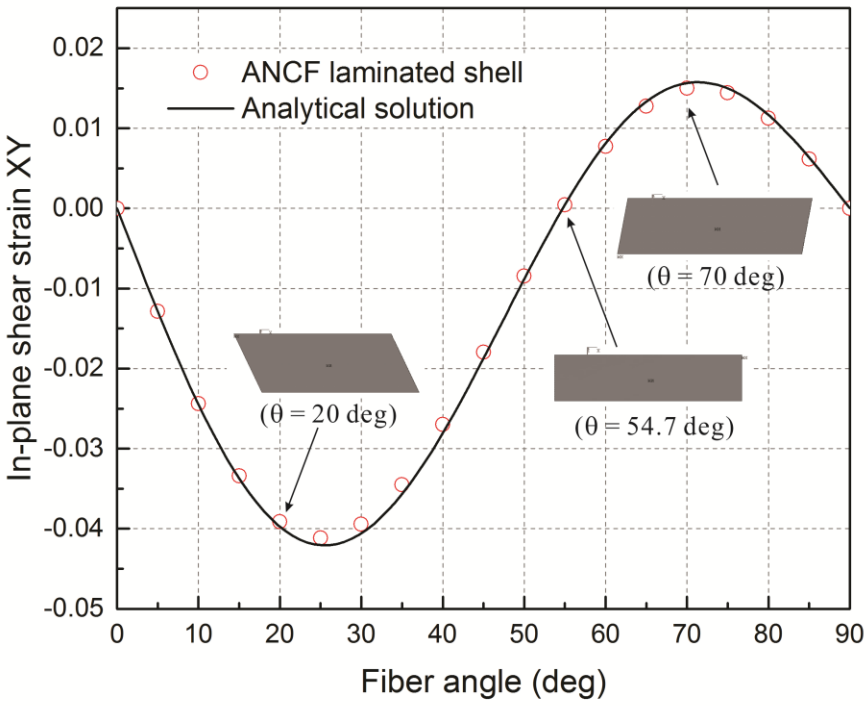


Figure 3. In-plane shear strain of one-layer orthotropic plate

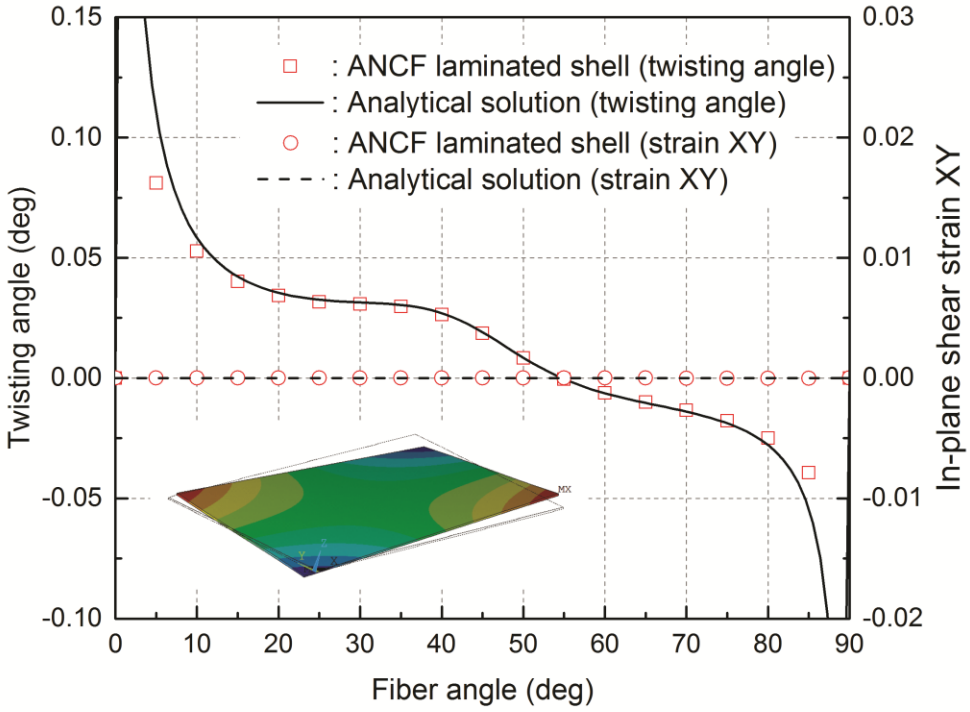


Figure 4. Twisting angle and in-plane shear strain of two-layer laminated composite plate subjected to uniaxial tensile load

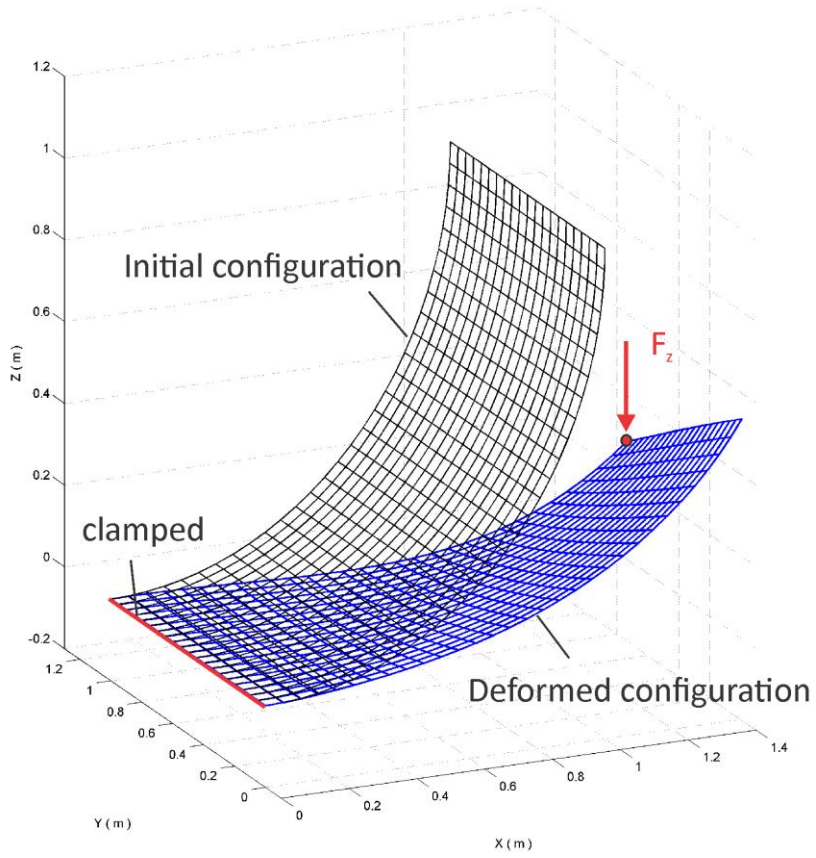


Figure 5. Deformed shape of cantilevered two-layer composite shell subjected to point load

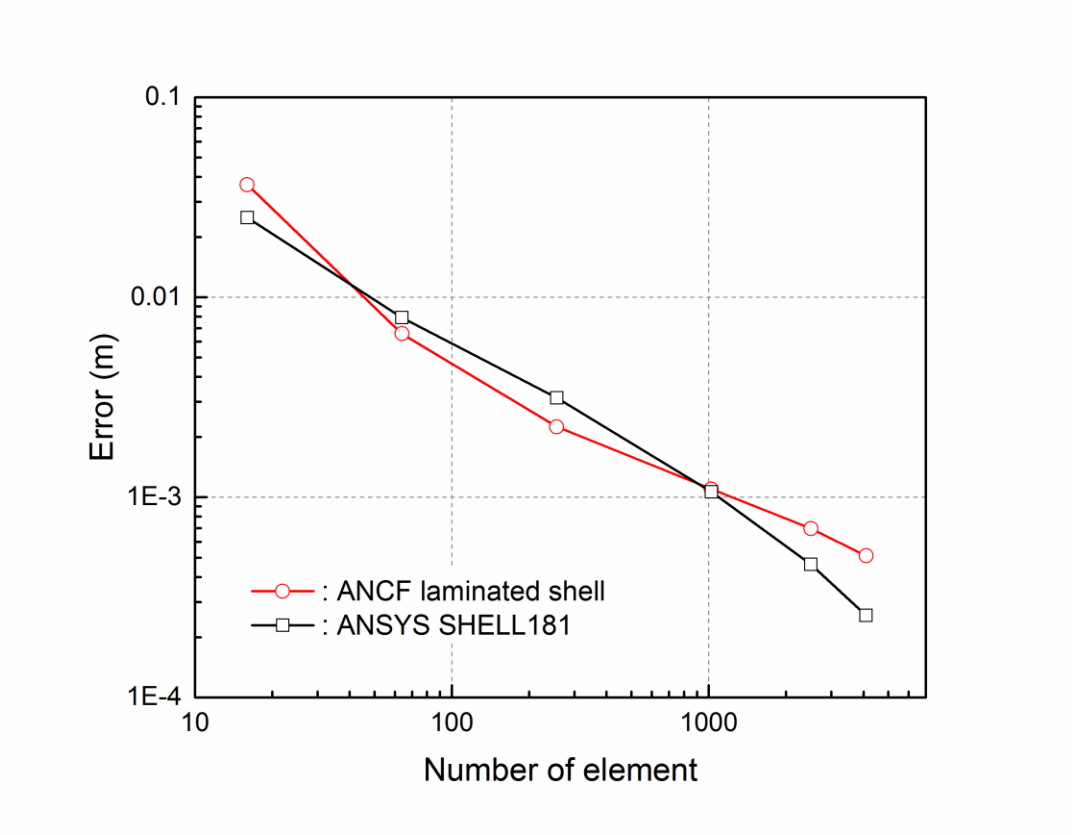


Figure 6. Numerical convergence of finite element solutions

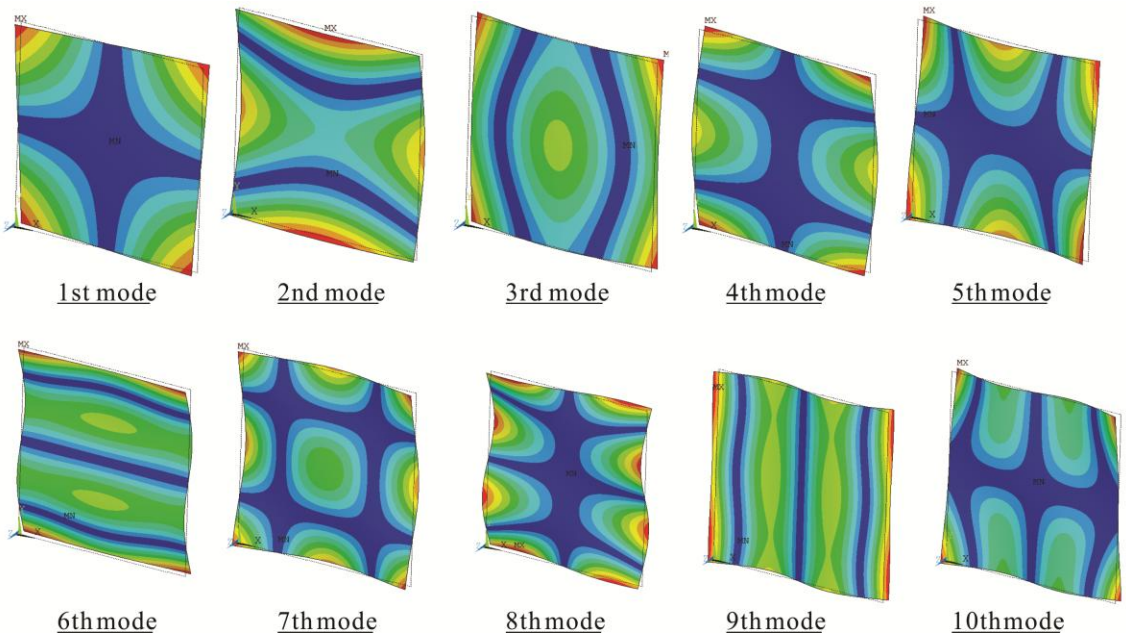


Figure 7. Vibration mode shapes of two-layer laminated composite shell

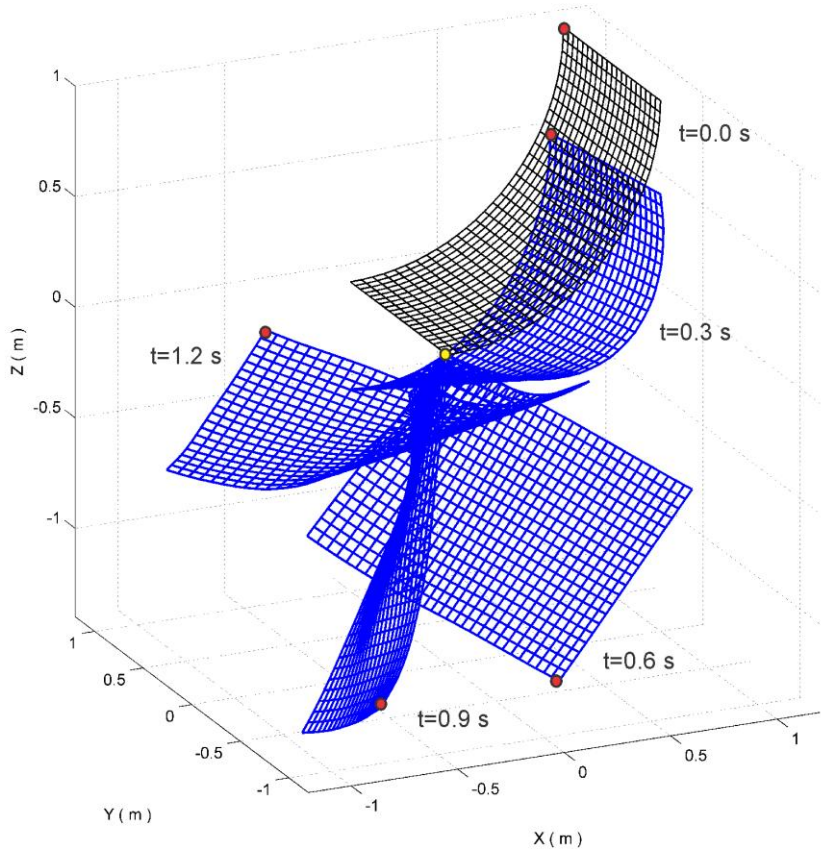


Figure 8. Deformed shapes

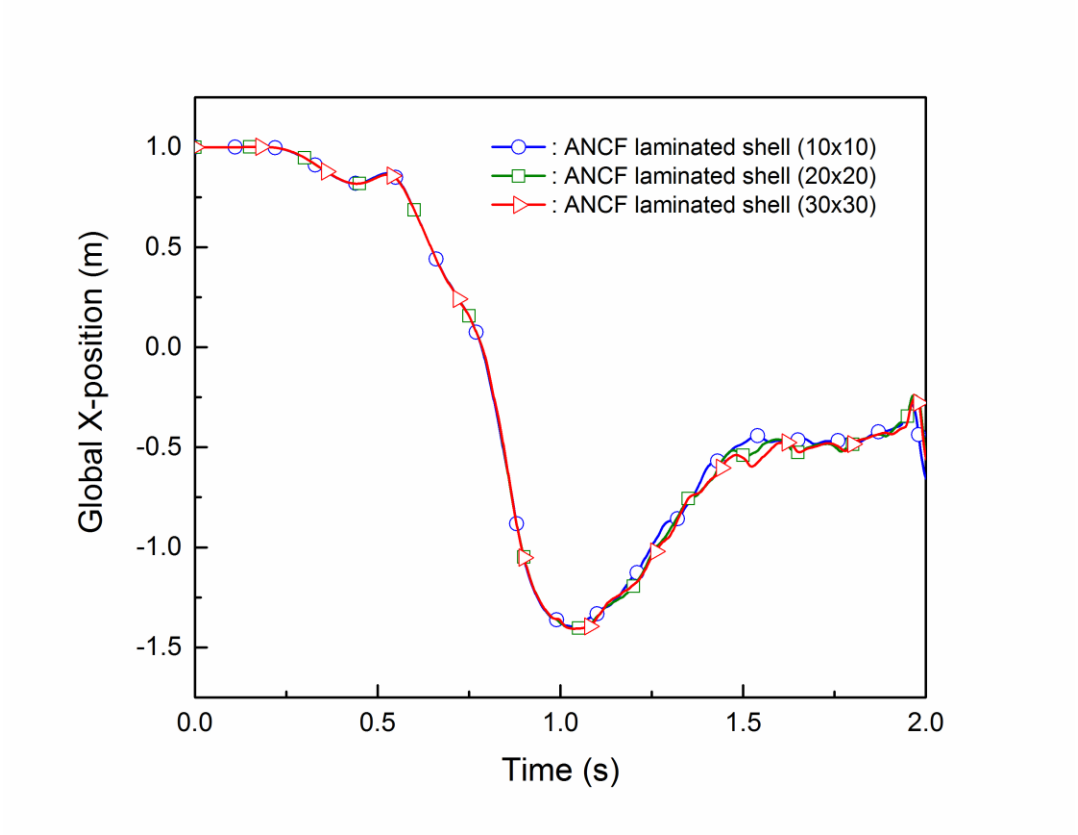


Figure 9. Global X-position at the tip point

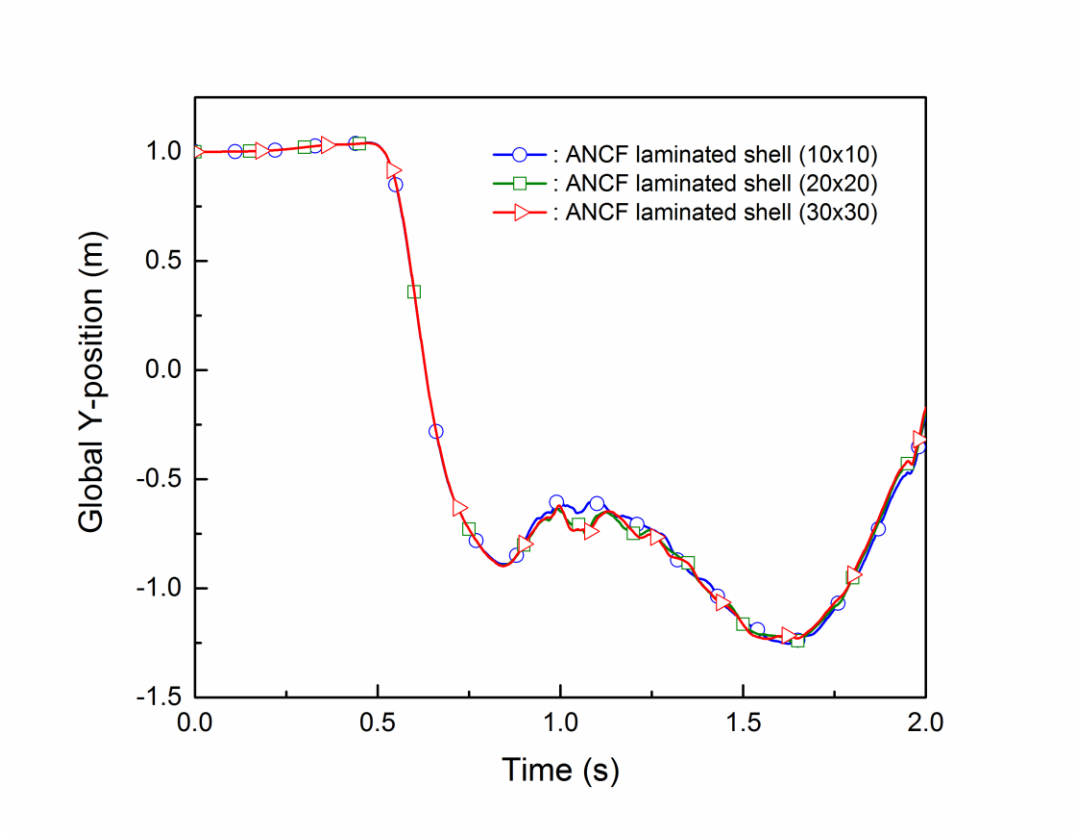


Figure 10. Global Y-position at the tip point

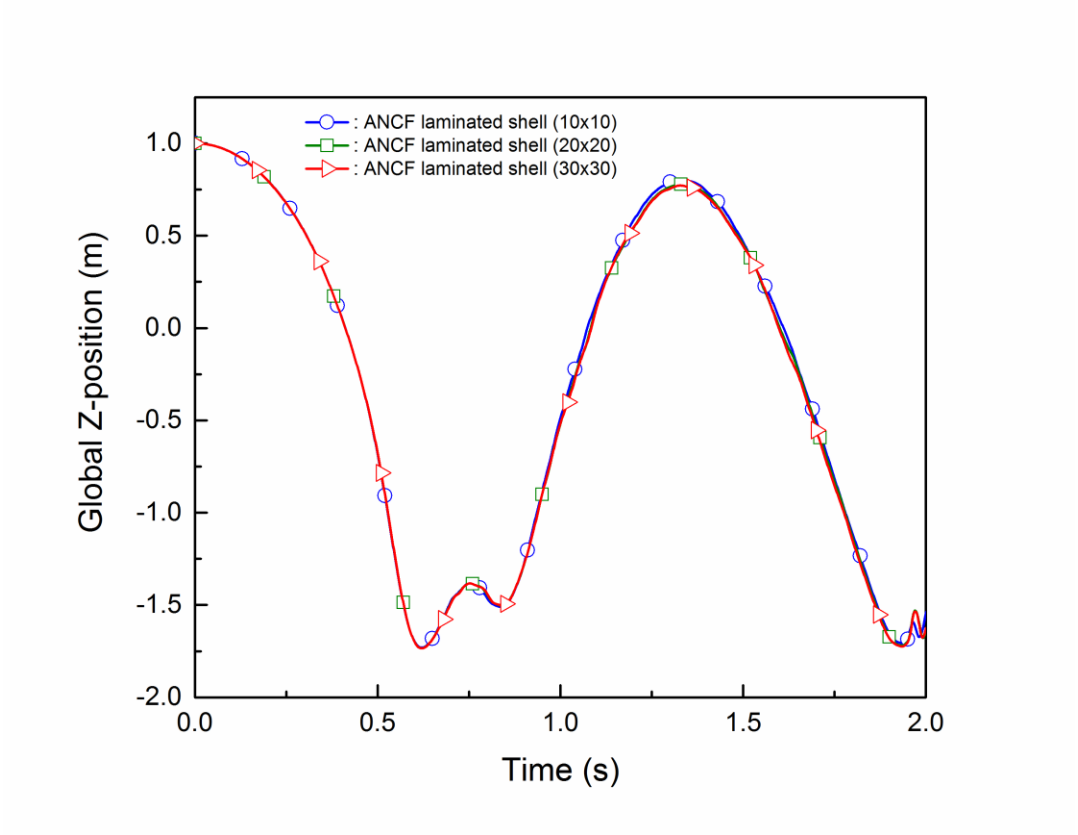


Figure 11. Global Z-position at the tip point

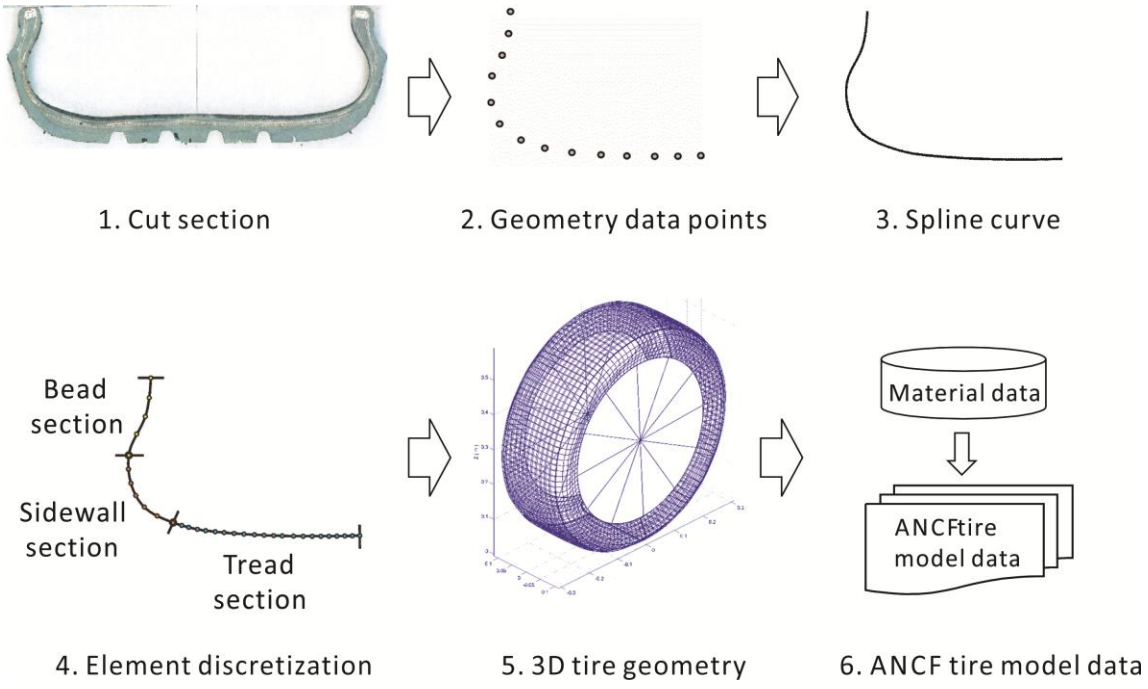


Figure 12. ANCF tire model creation procedure

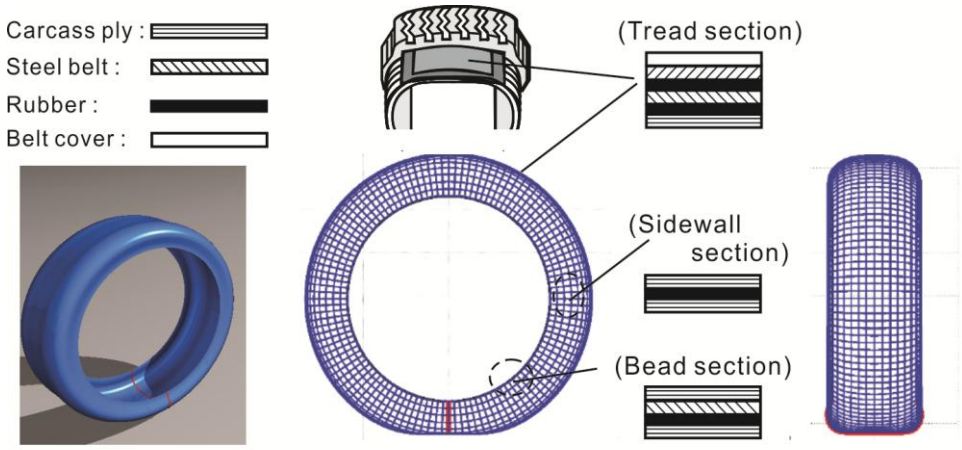


Figure 13. Physics-based ANCF tire model using multi-layered laminated composite shell element

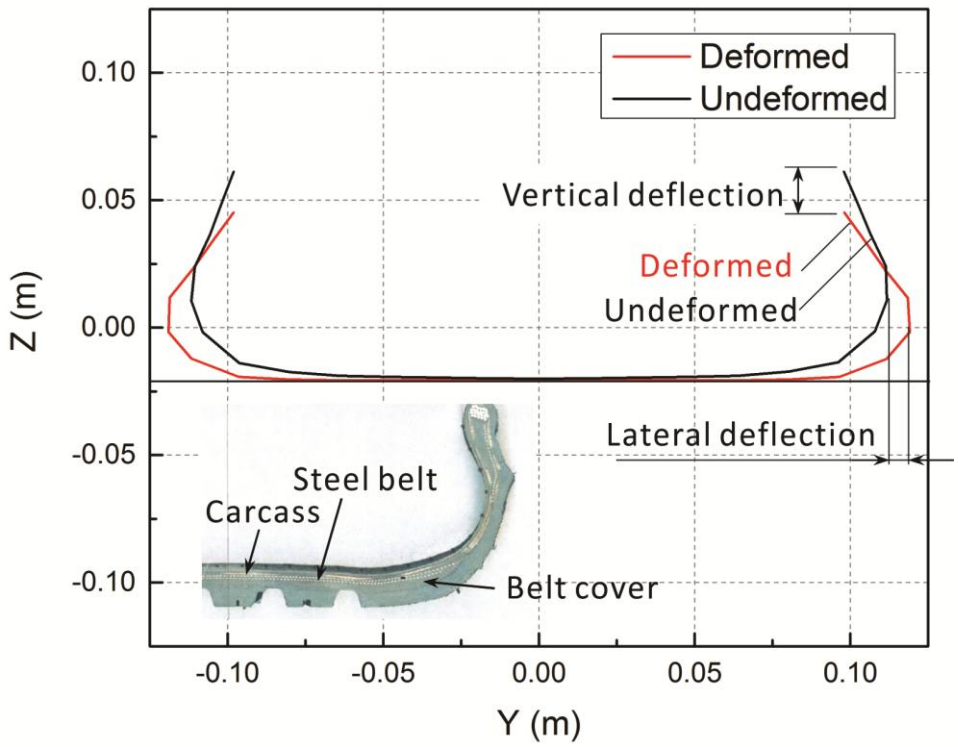


Figure 14. Deformed shape of tire cross section

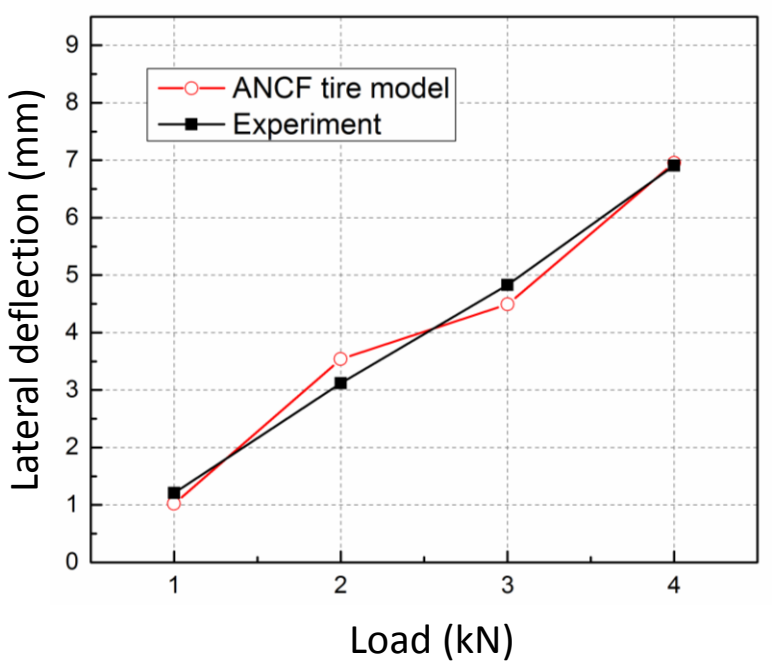


Figure 15. Lateral deflection of tire for various wheel loads

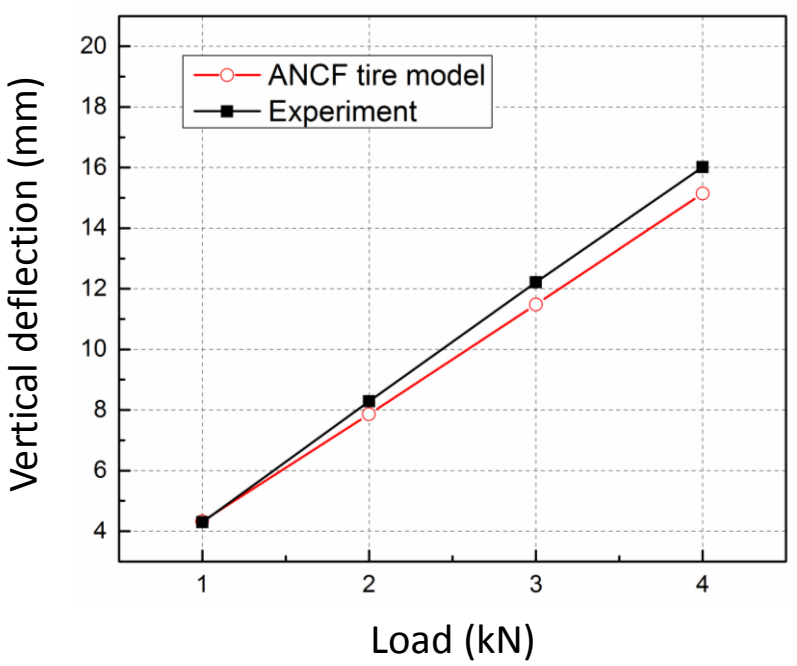


Figure 16. Vertical deflection of tire for various wheel loads

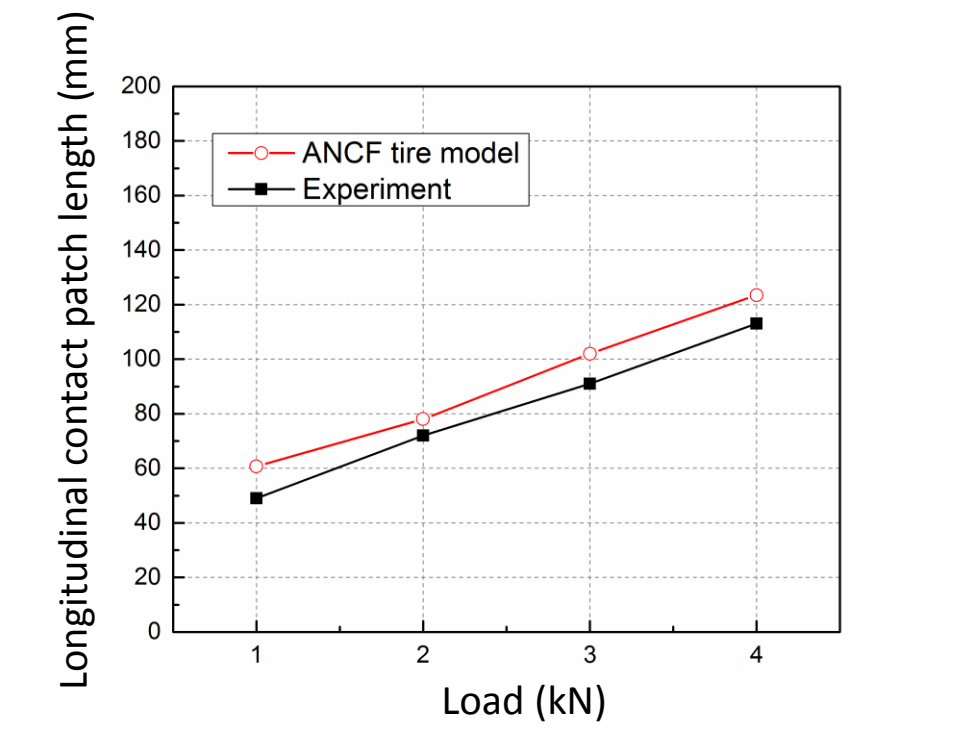


Figure 17. Longitudinal contact patch length for various wheel loads

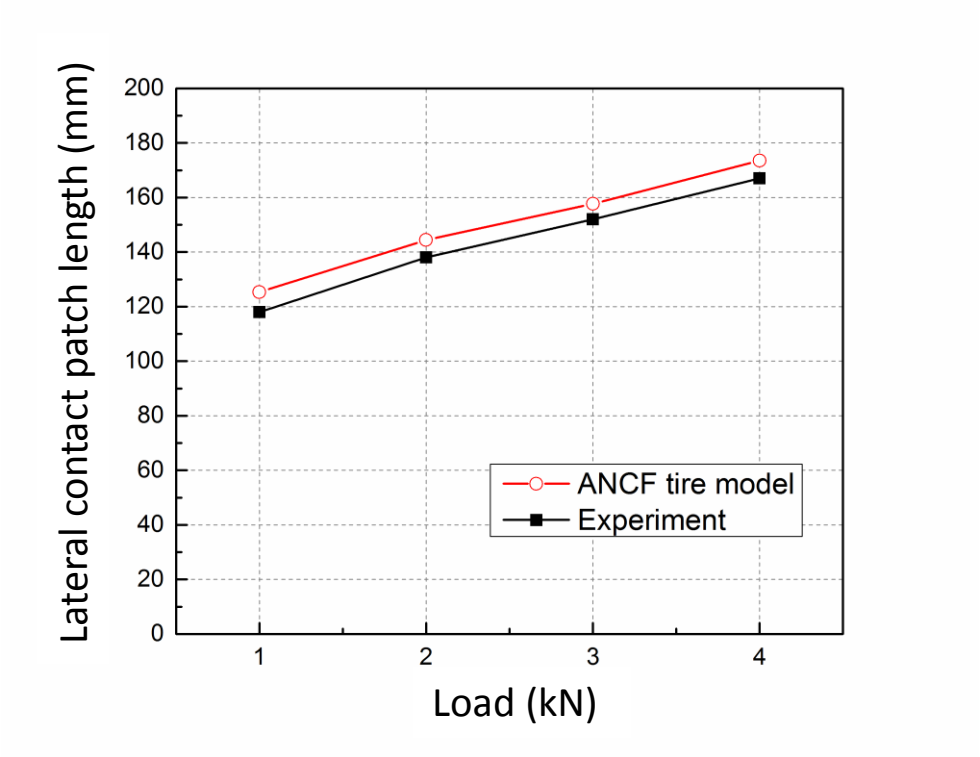


Figure 18. Lateral contact patch length for various wheel loads